

Bayesian inference of the dense matter equation of state built upon extended Skyrme interactions

Mikhail V. Beznogov^{1,*} and Adriana R. Raduta^{1,†}

¹*National Institute for Physics and Nuclear Engineering (IFIN-HH), RO-077125 Bucharest, Romania*

(Dated: March 29, 2024)

The non-relativistic model of nuclear matter with Brussels extended Skyrme interactions is employed in order to build, within a Bayesian approach, models for the dense matter equation of state (EOS). In addition to a minimal set of constraints on nuclear empirical parameters; the density behavior of energy per particle in pure neutron matter (PNM); a lower limit on the maximum neutron star (NS) mass, we require that the Fermi velocity of neutrons ($v_{F,n}$) in PNM and symmetric nuclear matter (SNM) with densities up to 0.8 fm^{-3} does not exceed the speed of light. The latter condition is imposed in order to cure a deficiency present in many Skyrme interactions [Duan and Urban, *Phys. Rev. C* 108, 025813 (2023)]. We illustrate the importance of this constraint for the posterior distributions. Some of our models are subjected to constraints on the density dependence of neutron (nucleon) Landau effective mass in PNM (SNM), too. The impact of various sets of constraints on the behaviors of nuclear matter and NSs is discussed in detail. When compared with models built upon standard Skyrme interactions, it turns out that those based on the extended interactions are stiffer if Fermi velocity is disregarded, but softer if it is taken into account.

I. INTRODUCTION

The equation of state (EOS) is an essential ingredient for describing systems as diverse as atomic nuclei, nuclear matter (NM) and neutron stars (NSs). The inability to infer it from first principle calculations of quantum chromodynamics make the phenomenological models the only practical solution. These models employ effective interactions, which are motivated by ab initio theory, but contain parameters adjusted by means of extensive fits of experimental data and theoretical calculations, and concentrate on self-consistent determination of the nuclear mean field.

In the past, NS EOSs have been obtained from EOSs of cold NM upon solving the β -equilibrium equation, which determines the elementary composition of matter. Limited information away the nuclear saturation density, $n_{\text{sat}} \approx 0.16 \text{ fm}^{-3} \approx 2.7 \times 10^{14} \text{ g/cm}^3$, and isospin symmetry, i.e., with roughly equal number of neutrons and protons, was reflected in a large scattering of the predictions of various models at densities in excess of a few times n_{sat} as well as in isospin asymmetric matter.

The advent of multi-messenger astrophysics of NSs has ushered in a renaissance of the topics of the EOS of dense matter [1–3]. As such, the observations of NSs with masses around or larger than $2 M_{\odot}$ [4–8] have been used as an argument in favor of a stiff EOS behavior at high densities, of particular relevance for an expected emergence of non-nucleonic particle degrees of freedom. Complementary information on the intermediate density behavior of neutron rich matter has been extracted from the measurement of tidal deformabilities of intermediate mass NSs, in the gravitational waves GW170817 event [9, 10]. Combined with radius inferences from fits of rotating hot spot patterns measured by NICER [11–13], and X-ray observations by XMM-Newton, these measurements contributed to tightening the EOS models over the density

range $1.5 \lesssim n/n_{\text{sat}} \lesssim 5$ and reduce by a factor of ~ 2 the error bars on radii measurements of PSR J0030+0451 and PSR J0740+6620, with masses of $\approx 1.4 M_{\odot}$ and $\approx 2.1 M_{\odot}$, respectively [14, 15].

The heterogeneity of constraints along with their dissimilar sensitivities to various density domains commends for an analysis where EOS models, built such as to maximally explore the parameter space of the model, are selected based on their ability to describe a set of constraints. The Bayesian statistics perfectly answers this requirement. A bulk of Bayesian inferences of the dense matter EOS has become available in the last couple of years, encompassing a wide selection of phenomenological models, including non-relativistic and relativistic mean field (RMF) models, and constraints. The RMF models with non-linear (NL) and density-dependent (DD) couplings have been used in Ref. [16–19] and Refs. [20–22], respectively; the non-relativistic mean field model with standard and extended Skyrme interactions has been employed in Refs. [18, 19, 23] and Ref. [18], respectively. The list of constraints implemented in various combinations in these studies include: nuclear empirical parameters (NEPs); energy per nucleon (E/A) and pressure (P) of pure neutron matter (PNM) with densities $n \lesssim n_{\text{sat}}$, as computed by ab initio models; nucleon and neutron effective masses at n_{sat} ; nuclear structure data, e.g., neutron skin thicknesses, dipole polarizability, masses; heavy ion collisions data, e.g., isospin diffusion, π -production, flow; a lower limit on the maximum NS gravitational mass; (combined) tidal deformability from GW170817 [9, 10]; NICER measurements of radii of PSR J0030+0451 and PSR J0740+6620 pulsars with estimated masses of $\approx 1.4 M_{\odot}$ and $\approx 2.1 M_{\odot}$ [11–14]; in the case of non-relativistic models, causality. In addition to NSs knowledge, translated either into confidence regions (CRs) in the pressure (P) – energy density (e) space, when it refers to the EOS, or posterior distributions of NS maximum gravitational mass, radii, tidal deformability or moments of inertia, when it refers to global observationally accessible parameters, these studies have addressed the issue of correlations among various parameters of NSs or with NEPs; model dependence of such correlations; modification of posterior distributions upon progressive incorporation of constraints; compatibility of

* mikhail.beznogov@nipne.ro

† araduta@nipne.ro

constraints coming from various sources.

Refs. [21, 23] allow one to contrast the results provided by the RMF model with DD couplings and the non-relativistic mean field model with standard Skyrme interactions, when EOS models are subjected to a *minimal set* of constraints. The conclusion is that NS EOSs based on standard Skyrme interactions are softer than those built based on the RMF with DD couplings, which makes that the NSs built within the first framework are characterized by values of radii and tidal deformability lower than those built within the second framework. A similar exercise, but with EOS models built within the RMF model with NL couplings and the non-relativistic mean field model with standard Skyrme interactions and subjected to a *comprehensive set* of constraints, which also includes data from NS observations and heavy ion collisions, has been performed in Ref. [19]. The conclusion of Ref. [19] is that accounting for astrophysical observations washes out to a considerable degree the model-dependence of the posteriors of the NS-related parameters, while this does not hold for NM posteriors and NS EOS. A remarkable results of Ref. [23] is that accounting for the correlations between the values that E/A in PNM takes at different densities not only brings further constraints into the isovector channel, but also couples it strongly to the isoscalar channel.

The aim of the present work is to pursue the investigation performed in Ref. [23], hereafter referred as Paper I. Several avenues are taken to this aim. First, instead of the standard Skyrme interaction, the Brussels extended Skyrme interaction is employed. In addition to an enhanced flexibility, due to a larger number of parameters of the effective interaction, this parametrization is expected to be able to provide for the density dependence of the Landau effective mass a behavior similar to the one predicted by ab initio calculations with three body forces [24, 25]. Second, the models we build comply with the requirement that up to a certain density, equal in our case to 0.8 fm^{-3} , the Fermi velocity of neutrons $v_{F,n}$ in both PNM and symmetric nuclear matter (SNM) does not exceed the speed of light. We mention that Duan and Urban [26] have recently signalled that many of widely used Skyrme parametrizations violate this condition, which obviously makes them unphysical.

Except for $v_{F,n}$, a set of constraints very similar to the one implemented in Paper I is adopted. More precisely, the constraints we implement correspond to the values of the four best known NEPs, i.e., n_{sat} , E_{sat} , K_{sat} and J_{sym} ; the density behavior of E/A and effective neutron mass in PNM ($m_{\text{eff};n}^{\text{PNM}}$) up to 0.16 fm^{-3} ; the density dependence of the effective nucleon mass in SNM ($m_{\text{eff};N}^{\text{SNM}}$) up to 0.16 fm^{-3} ; for the latter three quantities we use the results of χEFT calculations from Ref. [25]; a $2 M_{\odot}$ lower bound on the maximum gravitational mass of a NS. The obvious advantage of this strategy is that it allows a straightforward comparison between the results corresponding to standard and extended Skyrme interactions and, thus, highlights the role of extra momentum dependent terms. The consequences of the constraints on $v_{F,n}$ will be also considered. Minimal astrophysics input allows us to focus on the conditions related to nuclear experiments and theoretical calculations. Another important reason is that unlike the robust constraints on the lower limit of the maximum NS mass, radius-

related constraints should be treated with extreme care. As demonstrated recently by Vinciguerra et al. [27], NICER mass-radius estimates vary depending on noise setting and technical aspects of the inference procedure. Moreover, they show bi-modality. Constraints on tidal deformabilities from GW170817 event also depend on a number of assumptions like whether the same EOS was used for both NSs or not. Thus, we prefer not to include those constraints in our Bayesian analysis and only compare our results with those constraints a posteriori.

The rest of the paper is organized as follows. Sec. II briefly reviews the theoretical approach. The Bayesian setup is discussed in Sec. III. The behaviors of NM and NS matter are illustrated in Sec. IV along with detailed information about the model dependence of the results. The conclusions are drawn in Sec. V.

II. THE MODEL

In this paper we use the Brussels extended Skyrme interactions [28], which are obtained by supplementing the standard Skyrme interaction [29]

$$\begin{aligned} V(\mathbf{r}_1, \mathbf{r}_2) = & t_0 (1 + x_0 P_{\sigma}) \delta(\mathbf{r}) \\ & + \frac{t_1}{2} (1 + x_1 P_{\sigma}) [\mathbf{k}'^2 \delta(\mathbf{r}) + \delta(\mathbf{r}) \mathbf{k}^2] \\ & + t_2 (1 + x_2 P_{\sigma}) \mathbf{k}' \cdot \delta(\mathbf{r}) \mathbf{k} \\ & + \frac{t_3}{6} (1 + x_3 P_{\sigma}) [n(\mathbf{R})]^{\sigma} \delta(\mathbf{r}) \\ & + i W_0 (\boldsymbol{\sigma}_1 + \boldsymbol{\sigma}_2) \cdot [\mathbf{k}' \times \delta(\mathbf{r}) \mathbf{k}], \end{aligned} \quad (2.1)$$

with two density dependent terms,

$$\begin{aligned} V^{\text{BSk}}(\mathbf{r}_1, \mathbf{r}_2) = & V(\mathbf{r}_1, \mathbf{r}_2) \\ & + \frac{t_4}{2} (1 + x_4 P_{\sigma}) [\mathbf{k}'^2 [n(\mathbf{R})]^{\beta} \delta(\mathbf{r}) + \delta(\mathbf{r}) [n(\mathbf{R})]^{\beta} \mathbf{k}^2] \\ & + t_5 (1 + x_5 P_{\sigma}) \mathbf{k}' \cdot [n(\mathbf{R})]^{\gamma} \delta(\mathbf{r}) \mathbf{k}. \end{aligned} \quad (2.2)$$

In eqs. (2.1) and (2.2) the following notations are used: $\mathbf{r} = \mathbf{r}_1 - \mathbf{r}_2$, $\mathbf{R} = (\mathbf{r}_1 + \mathbf{r}_2)/2$; $\mathbf{k} = (\boldsymbol{\nabla}_1 - \boldsymbol{\nabla}_2)/2i$ is the relative momentum operator acting on the right and \mathbf{k}' is its conjugate acting on the left; $P_{\sigma} = (1 + \boldsymbol{\sigma}_1 \cdot \boldsymbol{\sigma}_2)/2$ is the two body spin-exchange operator; $n(\mathbf{r}) = n_n(\mathbf{r}) + n_p(\mathbf{r})$ is the total local density; $n_i(\mathbf{r})$ with $i = n, p$ are the neutron and proton local densities.

In the absence of spin polarization, the energy density of homogeneous matter with no Coulomb interaction is a sum of four terms

$$\mathcal{H} = k + h_0 + h_3 + h_{\text{eff}}, \quad (2.3)$$

where k is the kinetic energy term, h_0 is a density-independent two-body term, h_3 is a density-dependent term and h_{eff} is a momentum-dependent term. Each of these can be expressed in

terms of densities of particles and kinetic energies as

$$k = \frac{\hbar^2}{2m}\tau, \quad (2.4)$$

$$h_0 = C_0 n^2 + D_0 n_3^2, \quad (2.5)$$

$$h_3 = C_3 n^{\sigma+2} + D_3 n^\sigma n_3^2, \quad (2.6)$$

$$h_{\text{eff}} = \tilde{C}_{\text{eff}} n \tau + \tilde{D}_{\text{eff}} n_3 \tau_3, \quad (2.7)$$

where $n = n_n + n_p$ and $n_3 = n_n - n_p$ stand for the isoscalar and isovector particle number densities; $\tau = \tau_n + \tau_p$ and $\tau_3 = \tau_n - \tau_p$ denote the isoscalar and isovector densities of kinetic energy; $2/m = 1/m_n + 1/m_p$, where m_i with $i = n, p$ denotes the bare mass of nucleons.

The coefficients C_0 , D_0 , C_3 and D_3 have the same expressions as for the standard Skyrme interaction [30],

$$\begin{aligned} C_0 &= 3t_0/8, & D_0 &= -t_0(2x_0 + 1)/8, \\ C_3 &= t_3/16, & D_3 &= -t_3(2x_3 + 1)/48, \end{aligned} \quad (2.8)$$

while the contributions of extra terms enter into \tilde{C}_{eff} and \tilde{D}_{eff}

$$\begin{aligned} \tilde{C}_{\text{eff}} &= C_{\text{eff}} + [3t_4 n^\beta + t_5(4x_5 + 5)n^\gamma]/16, \\ \tilde{D}_{\text{eff}} &= D_{\text{eff}} + [-t_4(2x_4 + 1)n^\beta + t_5(2x_5 + 1)n^\gamma]/16, \end{aligned} \quad (2.9)$$

where

$$\begin{aligned} C_{\text{eff}} &= [3t_1 + t_2(4x_2 + 5)]/16, \\ D_{\text{eff}} &= [t_2(2x_2 + 1) - t_1(2x_1 + 1)]/16, \end{aligned} \quad (2.10)$$

are the coefficients of momentum-dependent interactions in the standard Skyrme [30]. With this convention there are 13 parameters (C_0 , D_0 , C_3 , D_3 , C_{eff} , D_{eff} , t_4 , x_4 , t_5 , x_5 , σ , β and γ) that define the most general form of Brussels extended Skyrme parametrizations. In practice the six parameters that enter Eq. (2.2) are given fixed values [28, 31, 32]. The advantages of doing so are in controlling the density dependence of the extra momentum dependent terms and keeping the χ^2 minimization procedure upon which the values of other parameters are obtained computationally cheap.

A peculiarity of the zero-range Skyrme interactions, where the momentum-dependent part of the potential is proportional to \mathbf{k}^2 , consists in the possibility of introducing effective masses

$$\frac{\hbar^2}{2m_{\text{eff};i}} = \frac{\hbar^2}{2m_i} + \tilde{C}_{\text{eff}} n \pm \tilde{D}_{\text{eff}} n_3, \quad (2.11)$$

that depend exclusively on particle densities; here “+” and “−” signs correspond to neutrons and protons, respectively. In the limit of zero temperature $m_{\text{eff};i}$ correspond to the Landau effective masses $m_{\text{Landau, eff};i}$, defined in terms of single particle density of states de_i/dk_i at the Fermi surface,

$$m_{\text{Landau, eff};i}^{-1} = \frac{1}{k_i} \left. \frac{de_i}{dk_i} \right|_{k=k_{F;i}}. \quad (2.12)$$

The presence of extra terms that depend on t_4 , x_4 , β , t_5 , x_5 , γ is essential for alleviating the decrease of $m_{\text{eff};i}$ with density.

As such, two major deficiencies can be healed. The first one regards the neutron Fermi velocity

$$v_{F;n} = \frac{k_{F;n}}{m_{\text{eff};n}} \quad (2.13)$$

that in dense matter might exceed the speed of light. Duan and Urban [26] have recently shown that this is a general issue with standard Skyrme interactions, which obviously makes them unsuitable for describing NS matter. Correlated with the previous aspect, the extra flexibility granted by the new terms can be exploited in order to achieve a $m_{\text{eff};i}(n)$ behavior compliant with the one predicted by microscopic models. Brueckner-Hartree-Fock calculations [24, 33] performed up to the density $n = 0.8 \text{ fm}^{-3}$ showed that three body (3N) forces are responsible for an U-shape behavior of $m_{\text{eff};i}(n)$. The minimum value of $m_{\text{eff};i}/m_N$ of the order of 0.7 was obtained for densities n ranging between 0.25 fm^{-3} and 0.6 fm^{-3} , depending on the strength of 3N forces and isospin asymmetry. χ EFT calculations [25] validate the qualitative findings of Refs. [24, 33], but predict that the minimum occurs at densities around n_{sat} . We also note that the extra momentum dependent terms lift the degeneracy that standard Skyrme interactions manifest for $\sigma = 2/3$.

The behavior of NM at arbitrary values of n and δ is commonly discussed in terms of NEPs. The first set of NEPs corresponds to the coefficients in the Taylor expansion of the energy per particle $E/A = \mathcal{H}/n = e/n$ in terms of the deviation $x = (n - n_{\text{sat}}^\delta)/3n_{\text{sat}}^\delta$ from the saturation density n_{sat}^δ ,

$$E(n, \delta)/A = \sum_{i=0,1,2,\dots} \frac{1}{i!} X_{\text{sat}}^{\delta;i} x^i, \quad (2.14)$$

with

$$X_{\text{sat}}^{\delta;i} = 3^i (n_{\text{sat}}^\delta)^i \left(\frac{\partial^i (e/n)}{\partial n^i} \right) \Big|_{n=n_{\text{sat}}^\delta}. \quad (2.15)$$

The (approximate) isospin invariance of the nucleon-nucleon interaction and the fact that SNM is more stable than isospin asymmetric matter allow for an alternative Taylor expansion, this time in terms of δ^2 [34],

$$E(n, \delta)/A = E_0(n, 0) + \delta^2 E_{\text{sym};2}(n, 0) + \delta^4 E_{\text{sym};4}(n, 0) + \dots \quad (2.16)$$

Here $E_0(n, 0)$ corresponds to the saturation density of SNM and $E_{\text{sym};k}$ stand for different order terms of the symmetry energy. Each of these can be further expanded in terms of the deviation $x = (n - n_{\text{sat}}^0)/3n_{\text{sat}}^0$ from the saturation density of SNM,

$$E_0(n, 0) = \sum_{i=0,1,2,\dots} \frac{1}{i!} X_{\text{sat}}^{0;i} x^i, \quad (2.17)$$

$$E_{\text{sym};k}(n, 0) = \sum_{j=0,1,2,\dots} \frac{1}{j!} X_{\text{sym};k}^{0;j} x^j, \quad k = 2, 4, \dots \quad (2.18)$$

where $X_{\text{sym};k}^{0;j} = \left(\partial^j E_{\text{sym};k}(n, 0) / \partial x^j \right) \Big|_{n=n_{\text{sat}}^0}$.

Table I. Constraints imposed on EOS models. E_{sat} and K_{sat} represent the energy per particle and compression modulus of symmetric saturated matter with the density n_{sat} ; J_{sym} stays for the symmetry energy at saturation; $(E/A)_i$ with $i = 2, 3, 4$ stand for the energy per particle of PNM at the densities of 0.08, 0.12 and 0.16 fm⁻³; $m_{\text{eff};n;i}^{\text{PNM}}$ ($m_{\text{eff};N;i}^{\text{SNM}}$) denotes the Landau effective mass of the neutron (nucleon) in PNM (SNM) at the density n_i ; M_G^* represents the maximum gravitational mass of a NS. For all quantities except M_G^* we provide the mean and its standard deviation; for M_G^* we specify the threshold values. m_n and m_N represent the neutron and nucleon bare masses, respectively.

Quantity	Units	Value	Std. deviation	Ref.
n_{sat}	fm ⁻³	0.16	0.004	1
E_{sat}	MeV	-15.9	0.2	1
K_{sat}	MeV	240	30	1
J_{sym}	MeV	30.8	1.6	1
$(E/A)_2$	MeV	9.212	0.226	2
$(E/A)_3$	MeV	12.356	0.512	2
$(E/A)_4$	MeV	15.877	0.872	2
$m_{\text{eff};N;2}^{\text{SNM}}$	m_N	0.715	0.011	2
$m_{\text{eff};N;3}^{\text{SNM}}$	m_N	0.667	0.012	2
$m_{\text{eff};N;4}^{\text{SNM}}$	m_N	0.638	0.013	2
$m_{\text{eff};n;2}^{\text{PNM}}$	m_n	0.877	0.004	2
$m_{\text{eff};n;3}^{\text{PNM}}$	m_n	0.866	0.011	2
$m_{\text{eff};n;4}^{\text{PNM}}$	m_n	0.880	0.026	2
M_G^*	M_\odot	> 2.0	—	3

References. Margueron *et al.* [35]; (2) Somasundaram *et al.* [25]; (3) Fonseca *et al.* [8].

For asymmetric NM, the lowest order term in δ^2 in eq. (2.16), called the symmetry energy, and the per-nucleon cost of converting SNM in PNM, called asymmetry energy, are of major interest. Their expressions are

$$E_{\text{sym};2}(n) = \frac{1}{2} \left. \frac{\partial^2 (e/n)}{\partial \delta^2} \right|_{n, \delta=0}, \quad (2.19)$$

and

$$E_{\text{asym}}(n) = E(n, \delta = 1)/A - E(n, \delta = 0)/A, \quad (2.20)$$

respectively.

The expressions of most frequently used NEPs are provided in Appendix A.

III. THE BAYESIAN SETUP

In this section we discuss the various constraints imposed on our EOS models and the procedure adopted to explore the parameter space.

A. Constraints

As in our previous works [21, 23], our strategy is to employ a minimum number of well-motivated constraints coming from

Table II. Synoptic view of constraints on $(E/A)_i$, $m_{\text{eff};N;i}^{\text{SNM}}$ and $m_{\text{eff};n;i}^{\text{PNM}}$ with $i = 2, 3, 4$ and Fermi velocity (v_F) whose implementation changes from one run to the others.

Run	$(E/A)_i$	correl.	$m_{\text{eff};N;i}^{\text{SNM}}$	correl.	$m_{\text{eff};n;i}^{\text{PNM}}$	correl.	$v_F; n$
0	✓	✓	—	—	—	—	✓
1	✓	—	—	—	—	—	✓
1*	✓	—	—	—	—	—	—
2	✓	—	✓	—	✓	—	✓
3	✓	—	✓	—	✓	✓	✓

nuclear physics data, χ EFT calculations of NM with densities up to n_{sat} and extreme isospin asymmetries and astrophysical observations of NSs. As such, quantities not yet constrained will span wide ranges, which is essential for potential correlations to manifest.

The constraints from nuclear physics data correspond to properties of NM close to saturation and are the following: saturation density of SNM (n_{sat}), energy per particle of saturated SNM (E_{sat}), compression modulus of saturated SNM (K_{sat}), and the symmetry energy (J_{sym}) at n_{sat} . Their values, listed in Table I, are those calculated by Margueron *et al.* [35], who considered a collection of 35 Skyrme interactions that are frequently employed in the literature.

The density behavior of PNM is constrained by the χ EFT data from Ref. [25], where nucleon-nucleon (NN) interactions computed at N³LO are supplemented by three nucleon (3N) interactions computed at N²LO. All our runs account for χ EFT predictions for E/A in PNM, which are sufficient for constraining the low density behavior of the isovector channel. Some of our runs also account for χ EFT results regarding the density behavior of $m_{\text{eff};n}^{\text{PNM}}$ and $m_{\text{eff};N}^{\text{SNM}}$. The former is expected to further constrain the isovector channel, while it remains to be seen whether the latter adds to stronger constraints in the isoscalar sector or, on the contrary, reveals tension with the values adopted for NM in the vicinity of ($n_{\text{sat}}, \delta = 0$). For all the quantities for which we use the predictions of χ EFT [25], constraints are imposed at three densities $n = 0.08, 0.12, 0.16$ fm⁻³. The availability of the results corresponding to six Hamiltonians in Ref. [25] makes it possible to account for correlations among the values that each of these quantities takes at different densities, which strengthen the constraints [23]. For the means and standard deviations (SDs) of $(E/A)_i$, $m_{\text{eff};n;i}^{\text{PNM}}$, $m_{\text{eff};N;i}^{\text{SNM}}$, see Table I. For the different manner in which these constraints are implemented, see Table II. We mention that in addition to the runs in Table II we also considered the case analogous to run 3 but with correlations among $m_{\text{eff};N;i}^{\text{SNM}}$ instead of correlations among $m_{\text{eff};n;i}^{\text{PNM}}$. As the results of this run were very similar to the results of run 2, they are not included in the following figures. Nevertheless, some comments will be offered in the end of Sec. IV.

Two extra constraints are added to both SNM and PNM to ensure that the models we generate are physical. Specifically, we ask that in SNM and PNM i) for densities $n \leq 0.8$ fm⁻³, $0 \leq m_{\text{eff};i}/m_N \leq 1$ with $i = n, p$, ii) unless otherwise explicitly mentioned, for densities $n \leq 0.8$ fm⁻³ the neutron Fermi

velocity ($v_{F,n}$) does not exceed the speed of light. The threshold density of 0.8 fm^{-3} was chosen somewhat arbitrarily as a compromise between extending the validity domain of the model and computational efficiency. Specifically, run 1* is a full analogue of run 1, but without Fermi velocity constraint.

In addition, NS EOSs are required to be i) stiff enough to produce maximum NS masses in excess of $2 M_\odot$, ii) thermodynamically stable ($P > 0$ and $dP/dn \geq 0$), iii) causal up to a density equal to the central density of the maximum mass configuration.

We note that usage of constraints similar to those implemented in Paper I, where standard Skyrme interactions have been employed, allows to reveal the model-dependence of the results. We are particularly interested in the role played by the extra momentum dependent terms of the extended interaction, on the one hand, and the condition on the Fermi velocity, on the other hand. As a matter of fact, posterior distributions of various sets of models built here will be systematically confronted with some of the posteriors from Paper I. We also note that a similar exercise, where results of standard Skyrme interactions were confronted with those of an RMF model with density dependent couplings [21], has been done in Paper I.

B. Likelihood

From the likelihood point of view, the quantities on which we impose conditions can be classified into three categories: uncorrelated, correlated and threshold ones. In this paper, NEPs are always considered as belonging to the first category. Depending on whether correlations between the values that $(E/A)_i$; $m_{\text{eff};n;i}^{\text{PNM}}$; $m_{\text{eff};n;i}^{\text{SNM}}$ take at different densities are accounted for or not, these quantities enter the second or the first category. Quantities whose values under specific conditions are used in order to accept or reject models proposed during the Monte Carlo exploration of the parameter space enter into the third category. Examples for this case are offered by the maximum NS mass, speed of sound, and Fermi velocity. Effective masses in PNM and SNM enter into the third category as well, but, depending on the run, they might also enter into the first and/or the second categories.

The log-likelihood function of the run q can be decomposed into three parts

$$\log \mathcal{L}_q = \log \mathcal{L}_{q,\text{uncorr.}} + \log \mathcal{L}_{q,\text{corr.}} + \log \mathcal{L}_{q,\text{thresh.}} \quad (3.1)$$

The log-likelihood function for the uncorrelated constraints reads

$$\log \mathcal{L}_{q,\text{uncorr.}} \propto -\chi_{q,\text{uncorr.}}^2 = -\frac{1}{2} \sum_{i=1}^{N_q^{\text{uncorr.}}} \left(\frac{d_i - \xi_i(\Theta)}{\mathcal{Z}_i} \right)^2, \quad (3.2)$$

where $N_q^{\text{uncorr.}}$ is the number of uncorrelated constraints; d_i and \mathcal{Z}_i stand for the constraint and its SD; $\xi_i(\Theta)$ corresponds to the value the model defined by the parameter set Θ provides for the quantity i . For the meaning and values of d_i and \mathcal{Z}_i , see Table I.

The log-likelihood function for correlated constraints reads

$$\log \mathcal{L}_{q,\text{corr.}} \propto -\chi_{q,\text{corr.}}^2 = -\frac{1}{2} \sum_{j=1}^{N_q^{\text{corr.}}} \sum_{r=1}^{\mathfrak{N}_j} \sum_{s=1}^{\mathfrak{N}_j} (\text{cov}^{-1})_{rs}^{(j)} \delta \xi_r^{(j)} \delta \xi_s^{(j)}, \quad (3.3)$$

where $N_q^{\text{corr.}}$ represents the number of correlated constraints; \mathfrak{N}_j is the number of “states” among which the correlations are accounted for; $\delta \xi$ stands for the difference between the value of the constraint and the value provided by the model and

$$\begin{aligned} \text{cov}_{rs} &= \frac{1}{P-1} \sum_{k=1}^P \xi_k(n_r) \xi_k(n_s) \\ &- \frac{1}{P-1} \sum_{k=1}^P \xi_k(n_r) \frac{1}{P-1} \sum_{k=1}^P \xi_k(n_s), \end{aligned} \quad (3.4)$$

is the covariance between the values of the quantity ξ computed at densities n_r and n_s . The index k in eq. (3.4) runs over the number P of individual calculations and we have taken into account the Bessel’s correction since the mean and the covariance are determined from the same sample. For χ EFT calculations in Ref. [25], which we use here, $P = 6$. As follows from Tables I and II, $\mathfrak{N}_j = 3$ and $N_q^{\text{corr.}} = 1$. The normalization factors in Eqs. (3.2) and (3.3) are disregarded because they are not relevant for sampling from the posterior distributions (as long as they do not depend on the input parameters, which they do not in our case).

The log-likelihood function for threshold constraints is

$$\log \mathcal{L}_{q,\text{thresh.}} \propto -\chi_{q,\text{thresh.}}^2 = \begin{cases} 0, & \text{condition satisfied} \\ -10^{10}, & \text{condition violated} \end{cases} \quad (3.5)$$

Our primary method of Bayesian inference was affine invariant Markov Chain Monte Carlo (MCMC). For the details of the implementation, employed software and analysis of convergence, see Appendix B. For a general discussion on how to treat constraints pertaining to physical quantities, see Section 3.2 of Ref. [21]. For the motivation and details of the implementation of correlations, see Supplemental Materials of Ref. [25].

C. Priors

For the same technical reasons as in Paper I, we employ “mixed” input parametrization. More precisely, instead of using as input parameters the 13 parameters of the effective interaction, we use three NEPs (n_{sat} , E_{sat} and J_{sym}) and 8 parameters of the effective interaction (D_3 , C_{eff} , D_{eff} , t_4 , t_5 , σ , β , γ), while the values of x_4 and x_5 are fixed to zero. The remaining parameters of the effective interaction, C_3 , C_0 and D_0 , are computed according to

$$\begin{aligned}
C_3 &= \frac{1}{\sigma n_{\text{sat}}^{\sigma+1}} \left\{ -E_{\text{sat}} + \frac{\hbar^2}{10m} \left(\frac{3\pi^2}{2} \right)^{2/3} n_{\text{sat}}^{2/3} - \left(\frac{3\pi^2}{2} \right)^{2/3} n_{\text{sat}}^{5/3} \left[\frac{2}{5} C_{\text{eff}} + \frac{3t_4}{80} (3\beta + 2) n_{\text{sat}}^\beta + \frac{t_5}{40} (3\gamma + 2) (5 + 4x_5) n_{\text{sat}}^\gamma \right] \right\}, \\
C_0 &= -\frac{1}{n_{\text{sat}}} \left\{ \left(\frac{3\pi^2}{2} \right)^{2/3} \frac{\hbar^2}{5m} n_{\text{sat}}^{2/3} + (\sigma + 1) C_3 n_{\text{sat}}^{\sigma+1} + \left(\frac{3\pi^2}{2} \right)^{2/3} n_{\text{sat}}^{5/3} \left[C_{\text{eff}} + \frac{9t_4}{80} \left(\beta + \frac{5}{3} \right) n_{\text{sat}}^\beta + \frac{3t_5}{80} (5 + 4x_5) \left(\gamma + \frac{5}{3} \right) n_{\text{sat}}^\gamma \right] \right\}, \quad (3.6) \\
D_0 &= \frac{J_{\text{sym}} - J_k}{n_{\text{sat}}} - D_3 n_{\text{sat}}^\sigma + \left(\frac{3\pi^2}{2} \right)^{2/3} n_{\text{sat}}^{2/3} \left[-\left(\frac{C_{\text{eff}}}{3} + D_{\text{eff}} \right) + \frac{1}{8} t_4 x_4 n_{\text{sat}}^\beta - \frac{1}{24} t_5 (5x_5 + 4) n_{\text{sat}}^\gamma \right],
\end{aligned}$$

with $J_k = \hbar^2/6m \left(3\pi^2/2 \right)^{2/3} n_{\text{sat}}^{2/3}$.

Table III. Domains of the priors.

Parameter	Units	Min.	Max.
n_{sat}	fm^{-3}	0.14	0.18
E_{sat}	MeV	-16.9	-14.9
J_{sym}	MeV	22.8	38.8
D_3	$\text{MeV fm}^{3+3\sigma}$	-3 000	3 000
C_{eff}	MeV fm^5	-500	2 000
D_{eff}	MeV fm^5	-1 000	2 000
t_4	$\text{MeV fm}^{5+3\beta}$	-8 000	3 000
t_5	$\text{MeV fm}^{5+3\gamma}$	-4 000	4 000
β	—	0.07	1.1
γ	—	0.07	1.1
σ	—	0.07	1.1

As can be seen from Eqs. (2.9), fixing the values of x_4 and x_5 to zero does not affect the behavior of \bar{C}_{eff} and \bar{D}_{eff} provided that the prior range for t_4 and t_5 is wide enough. In contrast, some loss of generality occurs because J_{sym} and t_4 become independent of each other, see Eqs. (A7) and (A12).

The domain we consider for σ , $0.07 \leq \sigma \leq 1.1$, is narrower than the one considered in Paper I, $0.01 \leq \sigma \leq 1.1$. While this limitation significantly simplifies the sampling, it has very limited impact on the posteriors, see Appendix B of Paper I.

The domains of the priors are presented in Table III. For the three NEPs the input ranges are identical to those used in Paper I; they cover 10 SDs symmetrically around the respective mean value, cf. Table I. For D_3 , C_{eff} , D_{eff} , t_4 and t_5 the ranges were chosen by the trial and error procedure to make the ranges as narrow as possible without (strongly) cutting the posterior. Unlike the situation of standard Skyrme, here the physical constraints on effective masses cannot be cast directly into the constraints on C_{eff} and D_{eff} as there are additional density-dependent terms there, see Eqs. (2.9) and (2.11). For β and γ we chose the same range as for σ .

We have employed uniform (uninformative) priors in the ranges provided in Table III.

IV. RESULTS

Before discussing our results, we briefly mention the fitting quality of our runs. For all runs expect run 3, the maximum a posteriori value of χ^2 is less than 1.0. For run 3 it is 3.2.

A. Nuclear Matter

The role that each constraint plays on NM is diagnosed following the modifications of conditional probability density corresponding to the energy per nucleon in SNM and PNM; E_{asym} , Eq. (2.20); $m_{\text{eff};N}^{\text{SNM}}$ and $m_{\text{eff};n}^{\text{PNM}}$, Eq. (2.11), as functions of number density, as previously done in Paper I. Though, at variance with Paper I, here only the density dependence of E_{asym} ; $m_{\text{eff};N}^{\text{SNM}}$; $m_{\text{eff};n}^{\text{PNM}}$ will be illustrated. The behavior of $E/A(n)$ in SNM and PNM will be nevertheless commented in detail.

Results pertaining to various runs in Table II are illustrated in Fig. 1 on subsequent rows. As in Paper I, the conditional probability density plots of the posterior distributions are normalized such that for any given density the total probability is 1.0. The color map is normalized accordingly, with the black color corresponding to the maximum probability density at each given n .

The largest dispersion in $(E/A)_{\text{SNM}}$ (not shown), $(E/A)_{\text{PNM}}$ (not shown), E_{asym} (right), $m_{\text{eff};N}^{\text{SNM}}$ (left) and $m_{\text{eff};n}^{\text{PNM}}$ (middle column) are obtained for runs 1* and 1, which are the least constrained runs.

Accounting for correlations among $(E/A)_i$ in PNM (run 0) results in the suppression of models with extreme behaviors of $(E/A)_{\text{PNM}}$ as a function of density, with more impact on the stiffest models than on the softest ones. As a stiff behavior of PNM relates to large values of $(\bar{C}_{\text{eff}} + \bar{D}_{\text{eff}})$, by eliminating stiff PNM models, some of the stiff SNM models, characterized by large values of \bar{C}_{eff} , are also eliminated. Indeed, the 95% quantile of $(E/A)_{\text{SNM}}$ and the median in run 0 become less steep than in run 1; the 90% confidence interval (CI) band gets narrower. As a result, the curves corresponding to $E_{\text{asym}}(n)$ get concentrated in a narrower band; the 95% quantile and median also move to lower values.

Upon imposing constraints on the Fermi velocity, Eq. (2.13), the models with strong increase of E/A in both PNM and SNM as a function of density are disfavored. The situation is understandable given that i) the upper limit on v_F translates into a lower limit on effective masses, and ii) large values of $(E/A)_{\text{PNM}}$ [$(E/A)_{\text{SNM}}$] require large values of $(\bar{C}_{\text{eff}} + \bar{D}_{\text{eff}})$ [\bar{C}_{eff}] that, in turn, lead to low values of $m_{\text{eff};n}^{\text{PNM}}$ [$m_{\text{eff};N}^{\text{SNM}}$]. Soft models of $(E/A)_{\text{SNM}}$ are disfavored as well. The impact of $v_{F;n}$ on $E_{\text{asym}}(n)$ is particularly strong, run 1 featuring a less pronounced increase with n than run 1*.

The comparison with the results produced by standard Skyrme interactions under similar constraints, i.e., run 1* here vs run 1 in Paper I, allows one to see that i) the increase of

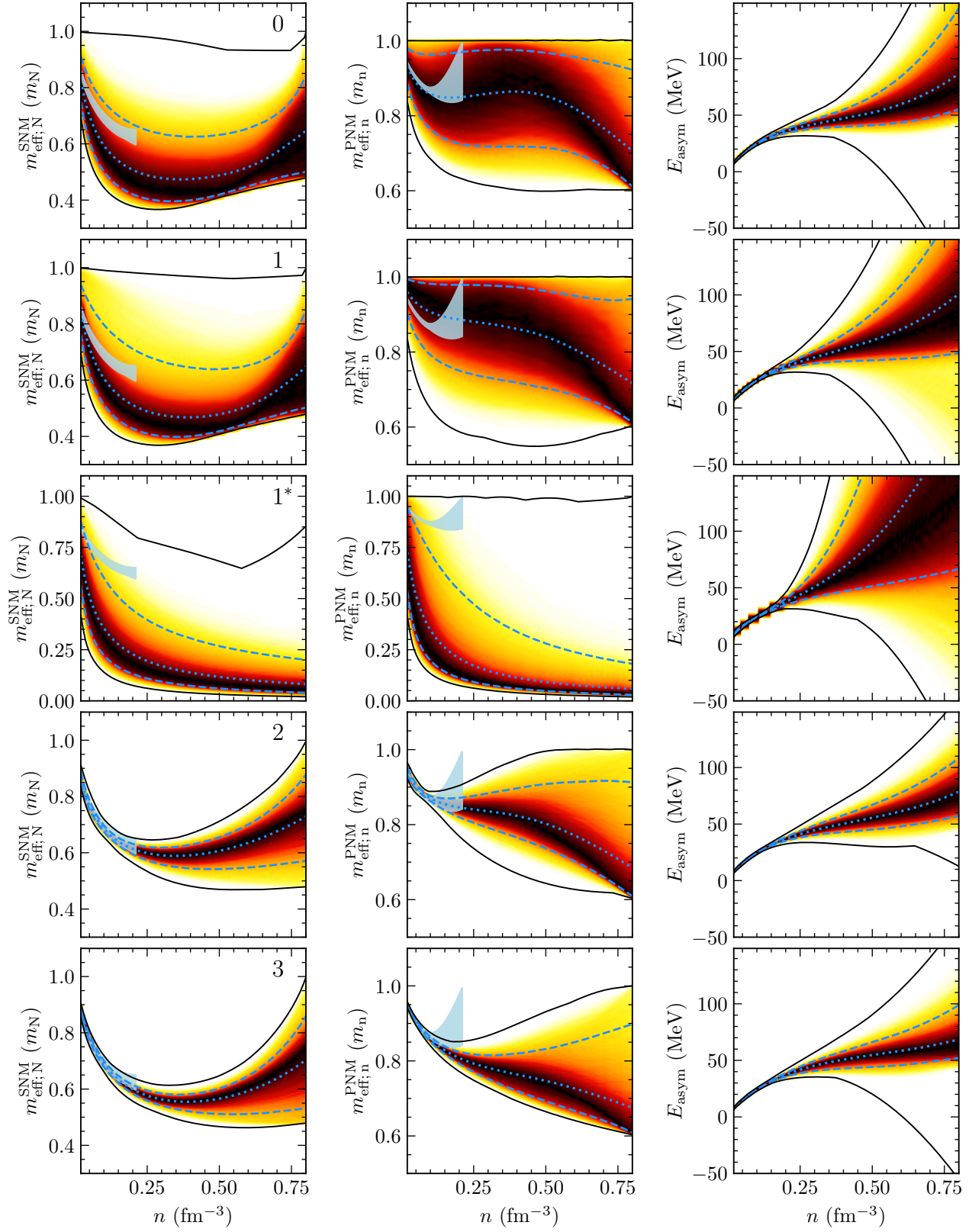


Figure 1. Conditional probability density (also known as curve density) plots corresponding to the density dependence of the asymmetry energy, Eq. (2.20), (right column), the nucleon effective mass in SNM (left column) and the neutron effective mass in PNM (middle column). Results of various runs are illustrated on subsequent rows, as indicated in the left panels. Curve density is indicated by colors: dark red (light yellow) corresponds to large (low) densities. Dotted and dashed dodger blue curves demonstrate the median and 90% CR, respectively. Solid black curves mark the envelope of the bunch of models associated with each run. Light blue shadowed regions mark the uncertainty domains, as computed in Ref. [25].

$(E/A)_{\text{PNM}}$ with density is much stronger for extended Skyrme than for standard Skyrme, ii) the increase of $(E/A)_{\text{SNM}}$ with density is slightly weaker for extended Skyrme than for standard Skyrme. In all present runs models providing E_{asym} increasing with density are dominant; this is in contrast with the results in Paper I, where a significant fraction of the models in each run allowed E_{asym} to become negative at high densities.

Left and middle columns in Fig. 1, where the behavior of $m_{\text{eff};N}^{\text{SNM}}$ and $m_{\text{eff};n}^{\text{PNM}}$ as functions of density is investigated, show that for run 1* the decrease of effective masses with density is much stronger than for standard Skyrme, see Fig. 2 in Paper I, especially at low densities. This hints at a strong increase of $\bar{C}_{\text{eff}}(n)$ and $\bar{D}_{\text{eff}}(n)$. The condition $v_{F;n}/c \leq 1$ prevents m_{eff} from dropping too much. The increased flexibility of the functional allows for a saturation in the decrease of effective masses as functions of density. The figure shows that, for densities in excess of $2n_{\text{sat}}$, $m_{\text{eff};N}^{\text{SNM}}$ increases with n ; this behavior is in qualitative agreement with the predictions of microscopic models [24, 25, 33]. The behavior of $m_{\text{eff};n}^{\text{PNM}}$ is more spectacular in the sense that, at least for run 0, many models manifest a second extremum, followed by a steep decrease. For runs 0 and 1, where only constraints on $(E/A)_i$ in PNM are implemented, the uncertainty bands are large for both $m_{\text{eff};N}^{\text{SNM}}$ and $m_{\text{eff};n}^{\text{PNM}}$.

Implementation of constraints on $m_{\text{eff};N}^{\text{SNM}}$ ($m_{\text{eff};n}^{\text{PNM}}$) suppresses models with either too large or too low values for this quantity. The panel corresponding to run 1 in Fig. 1 shows, for instance, that the number of models with large values of $m_{\text{eff};N}^{\text{SNM}}$ is smaller than the number of models with low values of $m_{\text{eff};N}^{\text{SNM}}$. These models correspond to cases with extreme values of \bar{C}_{eff} ($\bar{C}_{\text{eff}} + \bar{D}_{\text{eff}}$), i.e., to models with the softest or stiffest behavior of SNM (PNM). Upon their elimination, the envelopes of $(E/A)_{\text{SNM}}(n)$ [$(E/A)_{\text{PNM}}(n)$] and $E_{\text{asym}}(n)$ shrink considerably. Accounting additionally for correlations among the values that $m_{\text{eff};n,i}^{\text{PNM}}$ takes at different densities (run 3) slightly favors models with stiffer increase of $E/A(n)$ in PNM and SNM, which results in an E_{asym} envelope intermediate between those of run 0 and run 2. For $m_{\text{eff};N}^{\text{SNM}}$ a good agreement with the data from Ref. [25], which is used as constraints, is obtained up to $n = 0.2 \text{ fm}^{-3}$. In what regards $m_{\text{eff};n}^{\text{PNM}}$, the situation is less good. For $n \lesssim 0.1 \text{ fm}^{-3}$, our data fit the constraints from Ref. [25] well, while at higher densities it undershoots the constraints. The explanation is straightforward: for $m_{\text{eff};N}^{\text{SNM}}$ the target χEFT band has roughly constant width, which means that all constraints contribute more or less equally. For $m_{\text{eff};n}^{\text{PNM}}$ the width of the target band is rapidly increasing with density, which results in low density ($\lesssim 0.08 \text{ fm}^{-3}$) constraints being significantly more important than the high density (0.16 fm^{-3}) ones. Then, our data also fail to provide $m_{\text{eff};n}^{\text{PNM}}$ that, for densities exceeding $\approx n_{\text{sat}}$, increases with density. Accounting for correlations among the values that $m_{\text{eff};n,i}^{\text{PNM}}$ takes at different densities further shrinks the uncertainty bands for densities $n \lesssim 0.5 \text{ fm}^{-3}$. In the end we mention that the run in which correlations among the values that $m_{\text{eff};N}^{\text{SNM}}$ takes at different densities are taken into account leads to a collection of models very similar to the one in run 2.

B. Neutron stars matter

We now turn to investigate the role that each set of constraints plays on the NS EOS. NS EOSs are obtained by smoothly matching the core and the crust EOSs. For the outer and inner crusts we adopt the models by Haensel, Zdunik and Dobaczewski [36] and Negele and Vautherin [37], respectively. The matching between crust and core EOSs is done at a density of about $n_{\text{sat}}/2$. We assume that the leptonic sector consists of both electrons and muons.

Basic properties of NS EOSs are addressed in Fig. 2. Left columns depict the density dependence of the speed of sound squared (c_s^2), defined as $c_s^2/c^2 = (dP/de)_{\text{fr}}$, where the subscript “fr” indicates that the derivatives have to be evaluated with the composition frozen. The composition of beta-equilibrated matter is considered in the right column in terms of proton fraction Y_p . As before, each row corresponds to one of the runs in Table II.

The models in the least constrained run (run 1) show, as expected, the largest dispersion. The extra constraints on effective masses mainly reduce the dispersion of $c_s^2(n)$ -curves at $n \gtrsim 3n_{\text{sat}}$. Accounting for correlations between the values that E/A in PNM takes at different densities slightly reduces the dispersion at $n \lesssim 2n_{\text{sat}}$. The narrowest uncertainty band at 90% CR corresponds to run 2; this is the situation where E_{asym} curves show the smallest dispersion. Runs 0 and 1 contain models that soften at densities $n \sim 4n_{\text{sat}}$, which makes that the lower boundary of the envelopes decreases with the density. The number of these models is nevertheless very small because the curves corresponding to the 5% quantiles still increase as functions of density. We also note that for densities exceeding a certain (model dependent) value, the slope of $c_s^2(n)$ tends to saturate. The strongest effect is seen for soft models in runs 0 and 1. None of the runs in Paper I presented this behavior. Comparison between results of runs 1 and 1* allows to judge the effect of the $v_{F;n}$ constraint. It comes out that this condition suppresses the models with extreme values of c_s^2 and Y_p .

The E_{asym} increase with n , shown by most of the models, see Fig. 1, makes that for a huge majority of EOS models, Y_p of β -equilibrated matter increases with the density. As such, at variance with the results of Paper I, here only a small fraction of models allow for NS cores made exclusively of neutrons. The uncertainty bands of all runs are still large, indicating that the isovector channel is not well constrained. The shadowed light blue bands mark the threshold of the direct URCA processes, $Y_{p;\text{DU}} = 1 / \left[1 + \left(1 + x_e^{1/3} \right)^3 \right]$, with $x_e = n_e / (n_e + n_\mu)$. It comes out that all runs accommodate models that allow for this fast cooling process to operate as well as models where this reaction is forbidden.

C. Model dependence of the result

Here we investigate further the way in which the various sets of constraints modify the NM and NS EOSs. The analysis is done by considering 1D marginalized posterior distributions of different quantities. Examined are: parameters of NM;

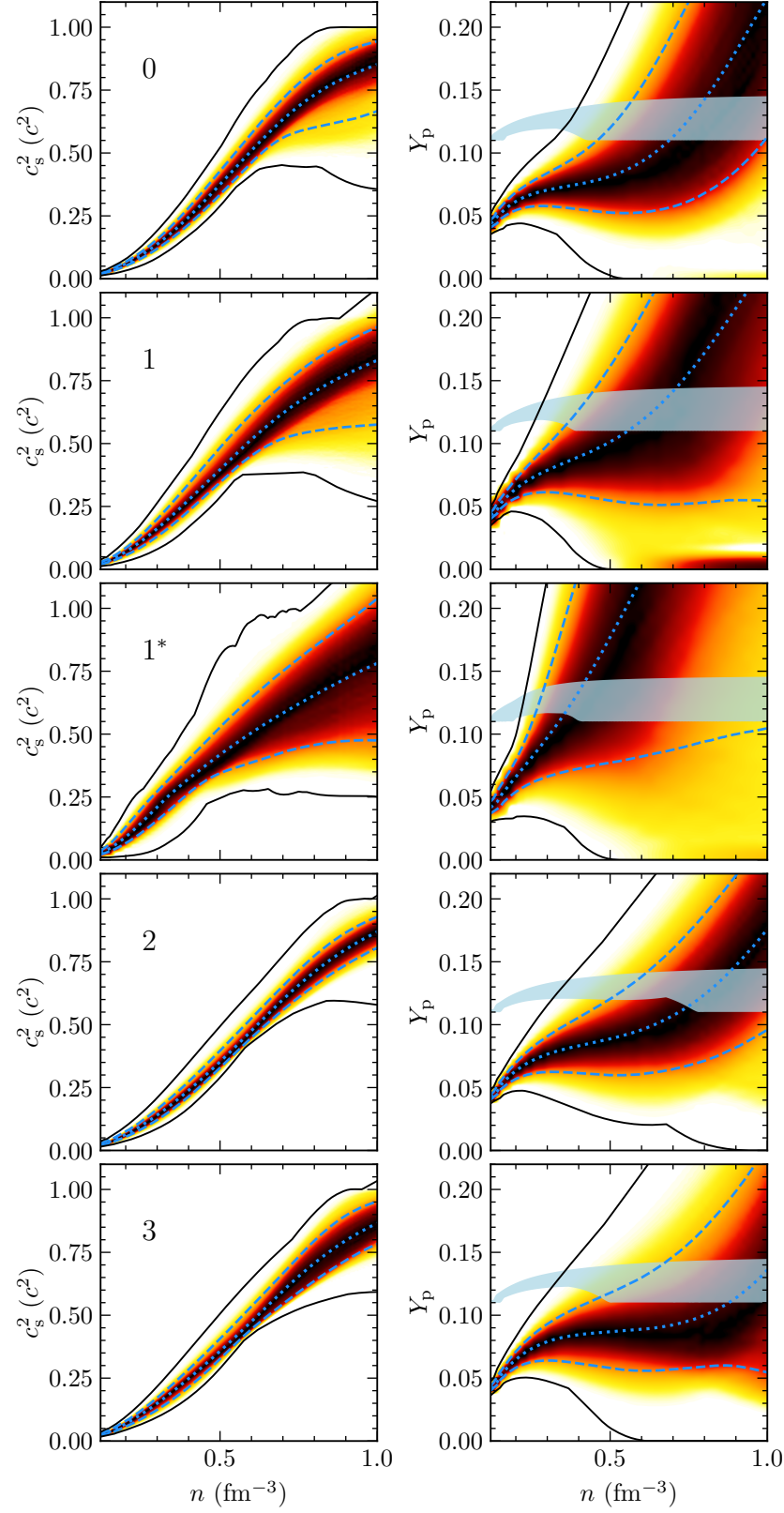


Figure 2. Conditional probability density (also known as curve density) plots corresponding to the density dependence of the speed of sound squared (left column) and proton fraction (right column) in NS matter. Results of various runs are illustrated on subsequent rows, as indicated on the left panels. The color map shows the curve density. Dotted and dashed dodger blue curves demonstrate the median and 90% CR, respectively. Solid black curves mark the envelope of the bunch of models associated with each run. The light blue domains on the right panels correspond to the direct URCA threshold, as predicted by our models; see text for details.

energy per particle in PNM with densities between 0.04 and 0.16 fm⁻³; neutron (nucleon) effective mass in PNM (SNM) with $n = 0.16$ fm⁻³; global parameters of NSs.

1. Posterior distributions of NM parameters; E/A in PNM and effective masses

Similarly to what was done in Paper I and for the same reason of improving the efficiency of the sampling, the MCMC exploration is performed by controlling n_{sat} , E_{sat} and J_{sym} , see Sec. III C. The first two quantities are allowed to take values in a narrow domain, see Table I. As such, their posterior distributions are confined and differ little from one run to the others. Posterior distributions of E_{sat} sit on the top of the target distribution; with the exception of run 1*, posterior distributions of n_{sat} are slightly shifted toward higher values. The latter result suggests that the constraint imposed on n_{sat} is in some tension with some of the constraints that govern the high density behavior, e.g., K_{sat} .

Posterior distributions of X_{sat}^i with $i = 2, 3, 4$ differ from one run to the others. The order of peaks' positions of K_{sat} distributions is opposite to the one of Z_{sat} distributions and similar to the one of Q_{sat} distributions. This is due to a strong and negative correlation between K_{sat} and Z_{sat} and a loose and positive correlation between K_{sat} and Q_{sat} , which was previously discussed in Refs. [17, 20, 21, 23] and seems to be a universal feature. Run 3 provides the narrowest distributions of K_{sat} and Z_{sat} . The narrowing of the K_{sat} distribution upon accounting for correlations among $m_{\text{eff};n}^{\text{PNM}}$ is the out-turn of the coupling between the isovector and isoscalar sectors. All the K_{sat} distributions miss the target distribution. The narrowest distributions of Q_{sat} are obtained for runs 0 and 2. The relative positions of K_{sat} and Z_{sat} posteriors corresponding to runs 1, 0 and 2 suggest that accounting for correlations among the values that E/A in PNM takes at different densities softens (stiffens) the EOS at densities slightly (a few times) higher than n_{sat} . X_{sat}^i distributions are almost identical for runs 0 and 2, which means that the constraints imposed on the density dependence of $m_{\text{eff};N}^{\text{SNM}}$ and $m_{\text{eff};n}^{\text{PNM}}$ have on the isoscalar channel effects similar to those of accounting for correlations among $(E/A)_i$ in PNM. Accounting for correlations among the values that $m_{\text{eff};n}^{\text{PNM}}$ takes at different densities shifts K_{sat} and Q_{sat} (Z_{sat}) distributions to larger (lower) values. Posteriors of run 3 are peaked at same values as posteriors of run 1 but are narrower.

Posterior distributions of J_{sym} are almost identical for runs 0 and 1 and runs 2 and 3. For runs 2 and 3 the peak value of J_{sym} fits the peak value of the target distribution. Posterior distributions of X_{sym}^i with $i = 1, \dots, 4$ are different from one run to the others. The narrowest distributions of L_{sym} corresponds to run 0; the narrowest distribution of Z_{sym} corresponds to run 3. These are the cases where the lowest (largest) peak values are obtained for L_{sym} (Z_{sym}), too. The fact that for $i = 1, \dots, 4$ X_{sym}^i distributions of run 0 are narrower than for run 1 confirms that accounting for correlations among E/A in PNM reduces the uncertainty band in the isovector channel. The effects of accounting for correlations among $m_{\text{eff};n}^{\text{PNM}}$ seem to be more important for high order terms in the Taylor expansion of the

symmetry energy than for low order terms.

The target distribution of $m_{\text{eff};N}^{\text{SNM}}$ at $n = 0.16$ fm⁻³ is met only when the behavior of this quantity is explicitly constrained, i.e., in runs 2 and 3. The target distribution of $m_{\text{eff};n}^{\text{PNM}}$ at $n = 0.16$ fm⁻³ is never met, even if the posteriors of runs 2 and 3 are narrow and closer to the χ EFT distribution than the posteriors of runs 0 and 1. As it was the case of $m_{\text{eff};n}^{\text{PNM}}(n)$ shown in Fig. 1, this is the out-turn of the uncertainty band in χ EFT calculations [25] that widens with density such that the constraints imposed at high densities are much less efficient than those imposed at low densities. $m_{\text{eff};N}^{\text{SNM}}$ distributions of runs 0 and 1 are identical. This means that, even if the isoscalar and isovector channels are coupled, the constraints on the isovector sector do not have repercussions on every property of SNM. $m_{\text{eff};n}^{\text{PNM}}$ distributions are different for runs 0 and 1 and both are wide. When compared with equivalent distributions corresponding to the standard Skyrme interactions, see Fig. 7 in Paper I, one notes that here effective masses are prevented from taking small values. This is the outcome of the constraint imposed on neutron Fermi velocity.

χ EFT distributions of E/A in PNM with densities equal to 0.04, 0.08 and 0.16 fm⁻³ are best described by run 0, which accounts for correlations among the values that this quantity takes at different densities. Even if no constraint is posed at $n = 0.04$ fm⁻³, it is at this density that the predictions of run 0 agree best with those of χ EFT [25]. We interpret this situation as the consequence of the uncertainty range of the E/A constraints, which widens with the density. In addition, one can see that run 0 here matches χ EFT results somewhat better than run 0 in Paper I (green shaded area). The peak value of $(E/A)_1$ agrees with the peak value of the corresponding χ EFT distribution also in run 1, though the posterior is much wider than the χ EFT reference. Note that for run 1 in Paper I (orange shaded area) the $(E/A)_1$ distribution misses the target distribution. The $(E/A)_4$ -distributions of runs 1 here and in Paper I are almost identical and narrower than the corresponding distribution of the more constrained run 0. Along with distributions of other runs, they span values higher than those of the χ EFT distribution. Accounting for extra constraints on $m_{\text{eff};n}^{\text{PNM}}$ and $m_{\text{eff};N}^{\text{SNM}}$ makes all the $(E/A)_i$ distributions in Fig. 3 deviate even more from the χ EFT distributions. Together with the way in which the different constraints modify the distributions of $m_{\text{eff};N}^{\text{SNM}}$ and $m_{\text{eff};n}^{\text{PNM}}$, this suggests that the flexibility introduced by the extra terms in the Brussels functional is not enough to match the density behavior of both E/A and m_{eff} in χ EFT calculations.

All X_{sat}^i , X_{sym}^i , $m_{\text{eff};n,i}^{\text{PNM}}$, $m_{\text{eff};N,i}^{\text{SNM}}$ and $(E/A)_i$ distributions are mono-modal. This situation is at variance with the one obtained in Paper I, where many of these quantities, e.g., K_{sat} , Q_{sat} , Z_{sat} , K_{sym} , Q_{sym} , Z_{sym} , $(E/A)_1$, $m_{\text{eff};N}^{\text{SNM}}$, show bimodal distributions. In the case of the standard Skyrme interactions the bimodality arises because the energy density functional becomes degenerate at $\sigma = 2/3$. The extra momentum dependent terms in extended interactions lift the σ -related degeneracy and, thus, suppress the bimodality. Shaded areas in Fig. 3, that correspond to runs 0 and 1 in Paper I, show that NEP distributions in this paper are, in most cases, narrower than those in Paper I. Considering that the interactions used here have more parameters than the interactions in Paper I, we attribute the

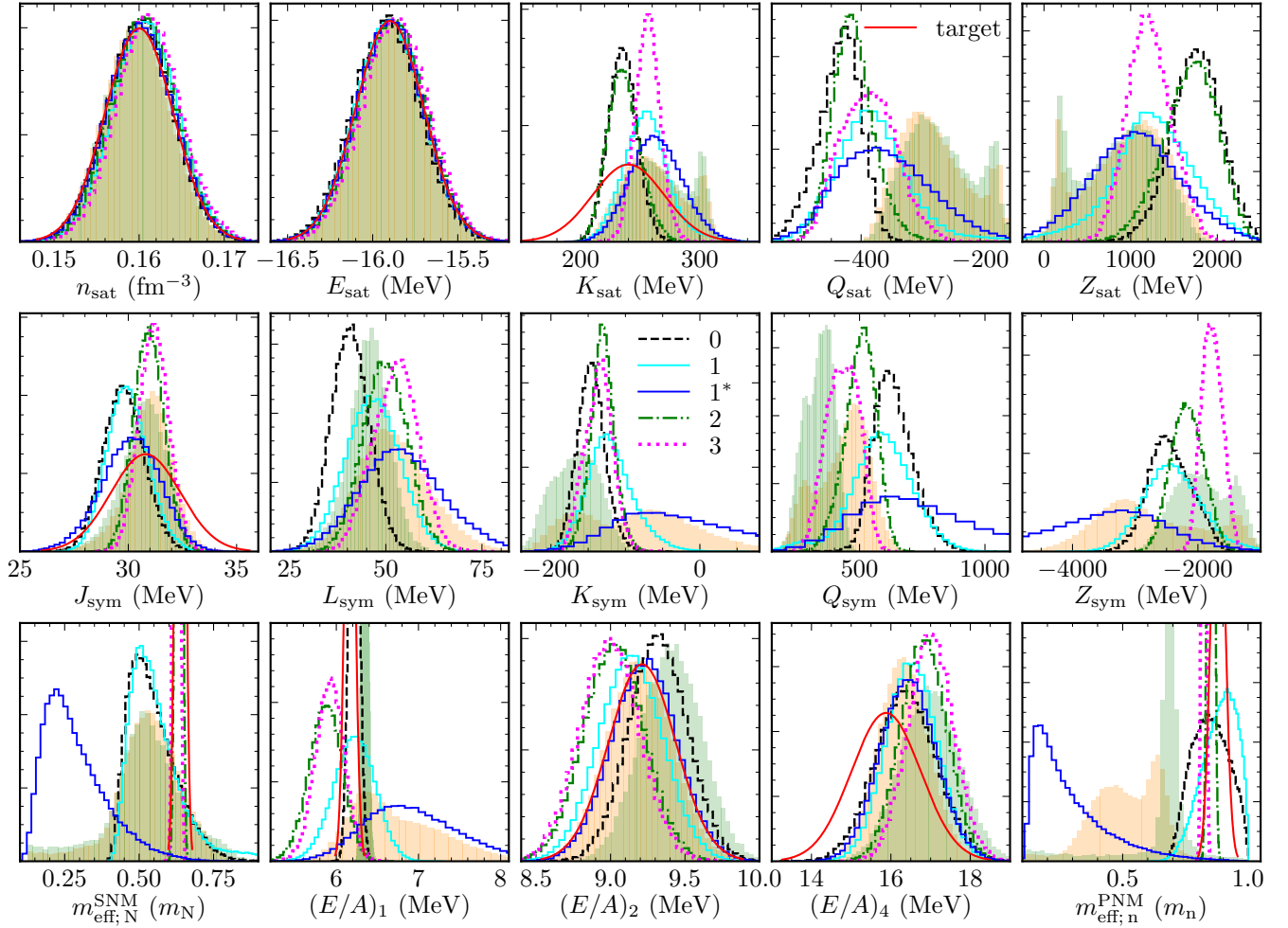


Figure 3. Marginalized posteriors of NEPs; effective nucleon mass in SNM with density $n = 0.16 \text{ fm}^{-3}$; effective neutron mass in PNM with density $n = 0.16 \text{ fm}^{-3}$ and energy per particle in PNM with densities $n = 0.04, 0.08$ and 0.16 fm^{-3} . All runs are considered. When available, target distributions for constrained parameters are also plotted. For comparison, marginalized posteriors corresponding to runs 0 and 1 in Paper I are illustrated as well (green and orange shaded areas, respectively). Y-axis ranges have been chosen to increase readability. As such, some of the very narrow distributions are cut.

better constraints of EOSs in this paper to the extra constraint on Fermi velocity. Further evidence in this sense is given by posteriors of run 1*.

When the constraint on the Fermi velocity [26] is removed, a larger portion of the parameter space becomes available. This translates into a larger variety of models and, thus, broader distributions of NEPs. The modification of the K_{sat} , Q_{sat} , and Z_{sat} posteriors with respect to run 1 is rather limited, which means that the isoscalar channel is not strongly limited by v_F constraints. The modification of X_{sym}^i with $i = 0, \dots, 4$ are more important and increase with the order in the expansion. For the first time, the target distribution of J_{sym} is described satisfactorily but this might be a coincidence. The fair agreement between L_{sym} distributions in this run and run 1 in Paper I might be fortuitous, too. The fact that the Q_{sym} and Z_{sym} distributions are wider than those of run 1 in Paper I is the consequence of a larger number of parameters in the effective interaction parametrization. The fair agreement between the $(E/A)_1$ dis-

tributions in run 1* here and run 1 in Paper I could be the out-turn of the fair agreement of L_{sym} and K_{sym} distributions. We remind that none of these runs posed constraints on the distribution of $(E/A)_1$. For the first time, the $(E/A)_2$ distribution perfectly fits the target distribution. The same holds for run 1 in Paper I. The $(E/A)_4$ distribution resembles the distributions in runs 0 and 1. This result is in line with those corresponding to X_{sat}^i . Distributions of $m_{\text{eff};n}^{\text{PNM}}$ and $m_{\text{eff};N}^{\text{SNM}}$ are wide and peaked at very low values, i.e., $\sim 0.2m_N$; this are the situations where the largest discrepancies are obtained with respect to the other runs here and in Paper I.

2. Posterior distributions of global NS parameters

Equilibrium configurations of static and spherically symmetric NSs are obtained by solving the Tolman-Oppenheimer-Volkoff equations. Tidal deformabilities are computed follow-

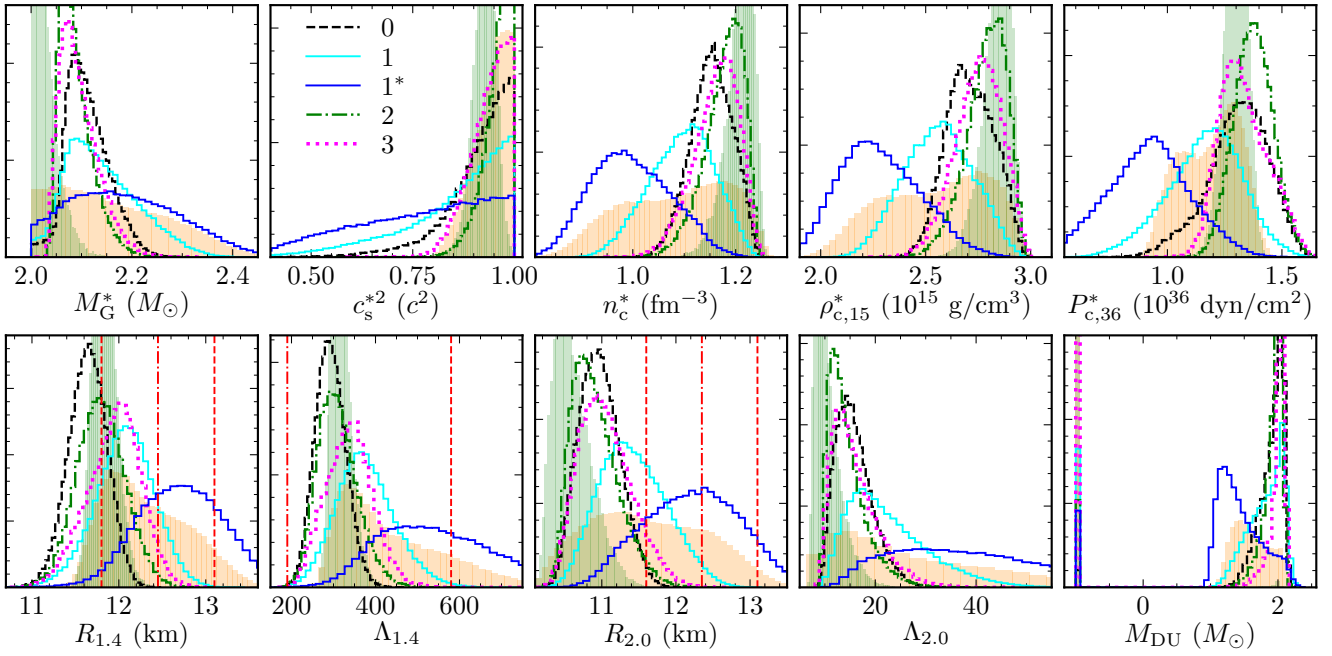


Figure 4. Marginalized posteriors of selected properties of NSs. Considered are: maximum gravitational mass (M_G^*); the central density corresponding to the most massive configuration (n_c^*); speed of sound squared (c_s^{*2}), energy density (ρ_c^*) and pressure (P_c^*) at n_c^* ; radii ($R_{1.4}$, $R_{2.0}$) and tidal deformabilities ($\Lambda_{1.4}$, $\Lambda_{2.0}$) of NSs with masses equal to $1.4 M_\odot$ and $2.0 M_\odot$; the lowest mass of a NS that accommodates for direct URCA (M_{DU}). The vertical dotted-dashed and dashed lines on the $R_{1.4}$ and $R_{2.0}$ plots illustrate the median and the lower and upper bounds (at 68% confidence), respectively, of the $R = 12.45 \pm 0.65$ km and $R = 12.35 \pm 0.75$ km constraints from Ref. [38]. The vertical dotted-dashed and dashed lines on the $\Lambda_{1.4}$ plot illustrate the median and the upper bound (at 90% confidence), respectively, of the 190^{+390}_{-120} constraint from Ref. [9]. For M_{DU} the value “−1” corresponds to the models that do not allow this process to operate in stable NSs. For comparison, marginalized posteriors corresponding to runs 0 and 1 of Paper I are illustrated as well (green and orange shaded areas, respectively). Y-axis ranges have been chosen to increase readability.

ing Refs. [39, 40].

Posterior distributions of a number of commonly considered global parameters of NS are illustrated in Fig. 4. Posterior distributions for runs 0 and 1 in Paper I are depicted for comparison. The 68% CI combined constraints [38] on the radii of $1.4 M_\odot$ and $2.0 M_\odot$ NSs are also shown on the corresponding panels. Constraints from GW170817 at 90% CI, as obtained in Ref. [9], are illustrated on the plot corresponding to the tidal deformability of a $1.4 M_\odot$ NS.

Posterior distributions of the maximum gravitational mass (M_G^*) are asymmetric and peaked at values in excess of $2.0 M_\odot$. In contrast, M_G^* distributions corresponding to runs 0 and 1 in Paper I peak at $2.0 M_\odot$, i.e., at the lower limit of the allowed maximum NS mass. Posterior distributions of the speed of sound squared at a density equal to the density of the maximum mass configuration (c_s^{*2}) lean on the maximum accepted value, c^2 . The c_s^{*2} distribution corresponding to run 0 of Paper I peaks at $\sim 0.9c^2$, while the one corresponding to run 1 is intermediate between distribution of run 0 of Paper I and those obtained here. When the constraint on $v_{F,n}$ is accounted for, the widest (narrowest) distributions of M_G^* and c_s^{*2} correspond to run 1 (2).

The explanation for the “dip” in the M_G^* distribution, which “shifts” the position of the peak, is that a significant number of models with the maximum mass close to the threshold value did not pass the criterion of having $c_s^{*2}/c^2 \leq 1$ and, thus,

have been suppressed. M_G^* distributions of runs 0 and 1 in Paper I manifest no “dip” and the respective c_s^{*2}/c^2 posteriors are peaked at values lower than c^2 . The posteriors of other quantities considered in Fig. 4, e.g., n_c^* , ρ_c^* , $R_{1.4}$, $R_{2.0}$, $\Lambda_{1.4}$, help to understand the reason of the discrepancy between present results and those in Paper I. Posteriors of n_c^* and ρ_c^* for run 0 in Paper I are concentrated in ranges that correspond to the highest values covered by the posteriors of the runs built here, which suggests that the EOSs in the run 0 in Paper I are softer than most of the EOS models we built here. This conclusion agrees with what the values of M_G^* in run 0 in Paper I, which are only slightly larger than $2 M_\odot$, and a c_s^{*2}/c^2 distribution peaked at $0.9 - 0.95$ convey. Posteriors of n_c^* and ρ_c^* for run 1 in Paper I are broad and bimodal, which suggests that there a bunch of soft models coexists with a bunch of stiff models. The bunch of soft (stiff) models leads to M_G^* values slightly (significantly) larger than the threshold value; low (large) values of $R_{1.4}$, $R_{2.0}$, $\Lambda_{1.4}$ and $\Lambda_{2.0}$.

The EOS models in runs 0, 2 and 3 have a tendency to be softer (stiffer) than most of the models corresponding to run 1 (0) in Paper I; the models in runs 1 and 1* are stiffer than those in run 0 in Paper I. The predictions of runs 0, 2 and 3 are relatively similar. Run 1, which is the least constrained, shows a wider range of behaviors. EOSs’ softness leads to $R_{1.4}$ and $R_{2.0}$ distributions that sit partially outside of the domains of

Ref. [38], which have been extracted based on a combination of pulsar timing data, X-ray data from NICER and XMM-Newton, GW data on tidal deformabilities and three theoretical frameworks of schematic EOS modelling. The disagreement with the data in Ref. [38] is more important for $R_{2.0}$ than for $R_{1.4}$. At variance with this, posteriors of $\Lambda_{1.4}$ for all runs except run 1* cover a domain delimited by the median and the upper boundary (at 90% CI) from Ref. [9].

When the very stringent constraint of the Fermi velocity [26] is relaxed, the characteristics of EOS models change drastically. All posteriors become wide. The EOS models become stiffer than when this constraint is imposed, which explains why many models provide for M_G^* values that exceed the threshold value by much. EOSs' stiffness also implies that distributions of n_c^* , ρ_c^* and P_c^* span values lower than those in the other runs. The positions of the peaks of the n_c^* and ρ_c^* posteriors roughly coincide with the positions of the low-density mode of the run 1 in Paper I. The fact that EOS models in run 1* are nevertheless different than those that make the “stiff bunch” of run 1 in Paper I is indicated by the P_c^* posterior, which does extend far beyond the range covered by the “stiff bunch” of run 1 in Paper I. In what regards $R_{1.4}$ and $R_{2.0}$, we note that the peaks are situated close to the median values from Ref. [38]. The peak of $\Lambda_{1.4}$ distribution is located somewhat below the 90% upper bound from Ref. [9] with $\approx 40\%$ of the posterior lying beyond this upper bound.

Fig. 4 also shows that all runs accommodate models that allow the direct URCA process to operate along with models where these reactions are forbidden. The percentages of models where the direct URCA acts in stable stars [stars with mass larger than $1.8 M_\odot$] are: 98.7 [75.9], 88.9 [51.9], 93.8 [15.1], 93.2 [79.4] and 69.6 [64.9] for run 0, 1, 1*, 2 and 3, respectively.

While there is no doubt that each constraint leaves imprints on every global parameter of NSs, the bunch of runs in this paper shows that the constraint on the Fermi velocity [26] is by far the strongest constraint.

In the end we mention that for all the “output” quantities plotted on Figs. 1 to 4 the posteriors of the run analogous to run 3 but with correlations between $m_{\text{eff};N;i}^{\text{SNM}}$ instead of $m_{\text{eff};n;i}^{\text{PNM}}$ are very close to the posteriors of run 2. However, the posteriors of the parameters of the effective interactions (not included here) are different from those of run 2. We explain the lack of effect of accounting for correlations among $m_{\text{eff};N;i}^{\text{SNM}}$ by the good constraint posed by individual values of $m_{\text{eff};N;i}^{\text{SNM}}$ in its turn, due to both narrow uncertainty band of χEFT data [25] and nearly constant width. The fact that different posteriors of the parameters of the effective interactions lead to almost identical “output” quantities illustrates inherent degeneracies of the energy density functional.

V. CONCLUSIONS

In this work we have performed a full Bayesian investigation of the dense matter EOS built upon the non-relativistic mean field model of nuclear matter with Brussels extended Skyrme interactions. Knowledge from nuclear structure experiments

was implemented via constraints on the values of the four best known NEPs, i.e., n_{sat} , E_{sat} , K_{sat} and J_{sym} . Knowledge from ab initio theoretical calculations of nuclear matter was incorporated via the density behavior of E/A and $m_{\text{eff};n}^{\text{PNM}}$ in PNM and the density behavior of $m_{\text{eff};N}^{\text{SNM}}$ in SNM, respectively, as computed in Ref. [25] based on χEFT with NN interactions computed at $N^3\text{LO}$ and 3N interactions computed at $N^2\text{LO}$. The behavior of neutron rich matter with densities in excess of several times n_{sat} was controlled by requiring that all EOS models comply with the $2 M_\odot$ constraint on the lower bound of the maximum NS gravitational mass. NS EOSs were also required to be thermodynamically stable, i.e., $P > 0$ and $dP/dn \geq 0$, and causal up to the density corresponding to the central density of the maximum mass configuration.

In addition to these, we implemented a condition that is mandatory for Skyrme models to be physical, but brought into attention only recently by Duan and Urban [26]. It consists in requiring that the Fermi velocity of nucleons in dense matter is inferior to the speed of light, which translates into a condition on the minimum value of the Landau effective masses. Our calculations show that this condition drastically changes the properties of NM and NSs. The density dependence of the Landau effective masses acquires a behavior that, up to the densities of the order of $2 - 3n_{\text{sat}}$, qualitatively reproduces the one predicted by ab initio calculations [24, 25, 33]. NS models become stiffer than when this condition is disregarded, which gets reflected in larger values of NS radii and tidal deformabilities as well as maximum NS gravitational masses in excess of $2.4 M_\odot$.

Families of EOS models have been built for various sets of constraints. In addition to accounting for correlations among the values that E/A in PNM takes at different densities, previously discussed in Paper I, here we have also considered the modifications brought by accounting for the correlations among the values that $m_{\text{eff};n}^{\text{PNM}}$ ($m_{\text{eff};N}^{\text{SNM}}$) in PNM (SNM) takes at different densities. The behavior of NM under different sets of constraints was analysed considering the behaviors of E/A and effective masses as functions of density in PNM and SNM as well as the density dependence of E_{asym} . As was easy to foresee, any extra condition on $m_{\text{eff};N}^{\text{SNM}}$ and/or $m_{\text{eff};n}^{\text{PNM}}$ helps to narrow down the uncertainty band of the EOS, especially at low densities. NS EOSs were investigated considering the density dependence of the speed of sound squared and Y_p . The model dependence of the results; the role of individual constraints; the effects of extra momentum dependent terms were judged upon by confronting the posterior distributions of various NM and NS quantities. For all the runs built here, the distributions of n_c^* extend up to densities exceeding 1.2 fm^{-3} , which are supposedly beyond the validity limit of the model. Strong core compression, typical to “soft” models, is reflected also in relatively low values of $R_{1.4}$, $\Lambda_{1.4}$ and $R_{2.0}$. Similarly to the case of standard Skyrme, all of the runs here contain models that allow for direct URCA to operate in stable stars.

It is particularly interesting to notice that, under identical constraints, some of the predictions of Brussels extended interactions differ from those of standard Skyrme interactions [23]: i) the overwhelming majority of Brussels interactions favor an (a)symmetry energy that increases with density, which trans-

lates into a Y_p of β -equilibrated matter also increasing with density; ii) stiffer NS EOS; iii) much lower values of $m_{\text{eff};N}^{\text{SNM}}$ and $m_{\text{eff};n}^{\text{PNM}}$ at 0.16 fm^{-3} ; iv) different distributions of Q_{sat} , K_{sym} , Q_{sym} , Z_{sym} . The last feature suggests that domains of values extracted by studying the behavior of either of these interactions should not a priori be imposed to the other.

The present paper is the follow-up of Paper I; the two papers aim to explore the capabilities of the non-relativistic mean field model with Skyrme interactions to describe NS matter. Together with Refs. [17, 20, 21], they contribute to a wider investigation of the high density behavior of phenomenological mean-field models with nucleonic degrees of freedom. Contrary to other Bayesian studies in the literature that also use mean-field models, e.g., Refs. [16, 18, 19, 22], we have preferred a minimum set of constraints and favored constraints from nuclear physics.

ACKNOWLEDGMENTS

We express our gratitude to Micaela Oertel for drawing into our attention physicality issues related to the Fermi velocity of the nucleons exceeding the speed of light at densities in excess of n_{sat} , which plague many Skyrme interactions [26].

Partial support from the Ministry of Research, Innovation and Digitization, Project No. PN 23 21 01 02 is acknowledged. M.V.B. and A.R.R. contributed equally to this work.

Appendix A: Nuclear Empirical Parameters

We provide here analytic expressions for low order NEPs. A hybrid set of parameters mixing the C_0 , D_0 , C_3 , D_3 , C_{eff} , and D_{eff} parameters, introduced in the standard Skyrme interactions in order to reduce the dimension of the parameter space relevant for the description of NM [30], with the t_4 , x_4 , t_5 , and x_5 parameters of the extra terms along with σ , β , and γ exponents that regulate the density dependence of the momentum dependent terms is employed. There are two arguments in favor of this choice. The first relates to the conciseness. More precisely, for each NEP, the expression corresponding to Brussels interactions X^{BSk} will be presented as a sum between a term entering the standard Skyrme interactions X^{Sk} , provided in Paper I, and extra terms specific to the extended interactions. The second argument pertains to the way in which the parameter space exploration is done numerically, see Sec. III. For equivalent expressions in terms of the most commonly used t_i , x_i with $i = 0, \dots, 4$ and σ , β , γ coefficients, see Ref. [41].

The saturation energy of NM with isospin asymmetry δ writes:

$$E_{\text{sat}}^{\text{BSk}}(\delta) = E_{\text{sat}}^{\text{Sk}}(\delta) + \mathcal{T}_4 + \mathcal{T}_5. \quad (\text{A1})$$

The corresponding expressions for incompressibility $K_{\text{sat}}(\delta) = X_{\text{sat}}^{\delta;2}$, skewness $Q_{\text{sat}}(\delta) = X_{\text{sat}}^{\delta;3}$ and kurtosis $Z_{\text{sat}}(\delta) = X_{\text{sat}}^{\delta;4}$ are:

$$K_{\text{sat}}^{\text{BSk}}(\delta) = K_{\text{sat}}^{\text{Sk}}(\delta) + (5 + 3\beta)(8 + 3\beta)\mathcal{T}_4 + (5 + 3\gamma)(8 + 3\gamma)\mathcal{T}_5, \quad (\text{A2})$$

$$Q_{\text{sat}}^{\text{BSk}}(\delta) = Q_{\text{sat}}^{\text{Sk}}(\delta) + (2 + 3\beta)(5 + 3\beta)(3\beta - 1)\mathcal{T}_4 + (2 + 3\gamma)(5 + 3\gamma)(3\gamma - 1)\mathcal{T}_5, \quad (\text{A3})$$

$$Z_{\text{sat}}^{\text{BSk}}(\delta) = Z_{\text{sat}}^{\text{Sk}}(\delta) + (3\beta - 4)(2 + 3\beta)(5 + 3\beta)(3\beta - 1)\mathcal{T}_4 + (3\gamma - 4)(2 + 3\gamma)(5 + 3\gamma)(3\gamma - 1)\mathcal{T}_5. \quad (\text{A4})$$

In the above expressions we made use of $\tau_i(T = 0) = \pi^{4/3} (3n_i)^{5/3} / 5$ and have introduced the notations:

$$\mathcal{T}_4 = \frac{3}{40} \left(\frac{3\pi^2}{2} \right)^{2/3} (n_{\text{sat}}^\delta)^{5/3+\beta} \left[t_4 (x_4 + 2) G_{5/3} - t_4 \left(x_4 + \frac{1}{2} \right) G_{8/3} \right], \quad (\text{A5})$$

$$\mathcal{T}_5 = \frac{3}{40} \left(\frac{3\pi^2}{2} \right)^{2/3} (n_{\text{sat}}^\delta)^{5/3+\gamma} \left[t_5 (x_5 + 2) G_{5/3} + t_5 \left(x_5 + \frac{1}{2} \right) G_{8/3} \right], \quad (\text{A6})$$

and $G_\alpha(\delta) = [(1 - \delta)^\alpha + (1 + \delta)^\alpha] / 2$.

The symmetry energy can be computed as

$$E_{\text{sym};2}^{\text{BSk}} = E_{\text{sym};2}^{\text{Sk}} + \mathfrak{T}_4 + \mathfrak{T}_5, \quad (\text{A7})$$

while its slope L_{sym} , curvature K_{sym} , skewness Q_{sym} and kurtosis Z_{sym} write

$$L_{\text{sym}}^{\text{BSk}} = L_{\text{sym}}^{\text{Sk}} + (5 + 3\beta)\mathfrak{T}_4 + (5 + 3\gamma)\mathfrak{T}_5, \quad (\text{A8})$$

$$K_{\text{sym}}^{\text{BSk}} = K_{\text{sym}}^{\text{Sk}} + (5 + 3\beta)(2 + 3\beta)\mathfrak{T}_4 + (5 + 3\gamma)(2 + 3\gamma)\mathfrak{T}_5, \quad (\text{A9})$$

$$Q_{\text{sym}}^{\text{BSk}} = Q_{\text{sym}}^{\text{Sk}} + (5 + 3\beta)(2 + 3\beta)(3\beta - 1)\mathfrak{T}_4 + (5 + 3\gamma)(2 + 3\gamma)(3\gamma - 1)\mathfrak{T}_5, \quad (\text{A10})$$

$$Z_{\text{sym}}^{\text{BSk}} = Z_{\text{sym}}^{\text{Sk}} + (5 + 3\beta)(2 + 3\beta)(3\beta - 1)(3\beta - 4)\mathfrak{T}_4 + (5 + 3\gamma)(2 + 3\gamma)(3\gamma - 1)(3\gamma - 4)\mathfrak{T}_5. \quad (\text{A11})$$

In the above expressions we have introduced

$$\mathfrak{T}_4 = -\frac{1}{8} \left(\frac{3\pi^2}{2} \right)^{2/3} t_4 x_4 n^{5/3+\beta}, \quad (\text{A12})$$

$$\mathfrak{T}_5 = \frac{1}{24} \left(\frac{3\pi^2}{2} \right)^{2/3} t_5 (5x_5 + 4) n^{5/3+\gamma}. \quad (\text{A13})$$

Notice that in Eqs. (A8) – (A11) the “0” superscript has been dropped off for convenience. The same convention is used throughout this paper.

Appendix B: MCMC implementation details

The general approach to the MCMC setup and its implementation here follow closely those described in Appendix B of Paper I. However, the higher dimensionality of the parameter space and the additional constraints on neutron Fermi velocity make the inference even more difficult.

We have employed `EMCEE` (v.3.1.4) Python package [42, 43]¹ as an implementation of the affine invariant MCMC [44] and as our main Bayesian inference tool. In all calculations we have used kernel density estimate (KDE) steps and 1 000 walkers. For the details of the two-stage inference procedure, autocorrelation length analysis and bootstrap analysis of the stability of the posteriors, see Appendix B of Paper I. Here we focus on what is different compared to Paper I.

First, due to the much higher computational cost of Bayesian inference for extended Skyrme, we had to thin the original chains less. If previously they were thinned up to the “thinned” autocorrelation length $\tau_{\text{th}} = 1.0 - 1.2$, here we only thinned the chains up to $\tau_{\text{th}} = 1.2 - 2.1$, thus reducing the number of independent samples in the posterior to $\gtrsim 48\%$ of the number of samples (in the worst case).

Second, for run 0 the autocorrelation length estimate was unreliable due to some of the walkers getting stuck for a large number of chain steps. Thus, for this run we decided to switch to `PTMCEE` sampler (v.1.0.0) [42, 45]² with tempered chains. Specifically, we employed 5 chains with the maximum temperature $T = 512$ and auto-adjusting temperatures for intermediate chains. The latter aimed to equalize the inter-chain swap probabilities, which were $\approx 30\%$. We made sure that even the highest temperature chain cannot “break through” the physical constraints on Fermi velocity and thermodynamic stability. With tempered chains the autocorrelation length is no longer an

issue as each chain swap almost entirely erases all intra-chain correlations; in other words, τ does not exceed the number of steps between two consecutive chain swaps. Nevertheless, even the highest temperature chain had low acceptance fraction ($\approx 15\%$) and advanced slowly, so we still had to thin the chains to compensate for this. With autocorrelation length no longer being a viable diagnostics, we used bootstrap analysis and the fraction of repetitions in the main chain as our diagnostic tools and to determine the necessary thinning factor. In particular, we thinned the chains until the fraction of repeated samples in the main chain dropped below $\lesssim 10^{-4}$.

In the same manner as in Paper I, to additionally verify the correctness of the results, the posterior for the most numerically problematic run (run 0) was calculated independently by means of a nested sampling [46, 47] algorithm `MLFriends` [48, 49], implemented in the Python package `ULTRANEST` (v.3.6.4) [50]³. We had to introduce minor custom adjustments to the algorithm responsible for the choice of initial positions of the live points. This was necessary to deal with likelihood plateaus occurring in the very beginning of the sampling as `ULTRANEST` default algorithm was inefficient for our problem. No other modifications were done. After $\approx 1.1 \times 10^{10}$ likelihood evaluations we ended up with $\approx 69\,000$ effective samples of the posterior (we employed inefficient, but robust region sampling). We have computed the values of 10%, 50% and 90% quantiles and compared `ULTRANEST` results against `PTMCEE` results. The maximum difference between the corresponding values did not exceed 6% and typical differences were less than 1%. Moreover, the maximum difference corresponded to a case where a quantile value was close to zero. Plotted on a figure, the histograms were very close.

Thus, we have confirmed that despite above-mentioned difficulties our results are reliable.

-
- [1] M. Oertel, M. Hempel, T. Klöhn, and S. Typel, Equations of state for supernovae and compact stars, *Rev. Mod. Phys.* **89**, 015007 (2017).
 - [2] G. F. Burgio, H. J. Schulze, I. Vidaña, and J. B. Wei, Neutron stars and the nuclear equation of state, *Prog. Part. Nucl. Phys.* **120**, 103879 (2021).
 - [3] S. Typel *et al.* (CompOSE Core Team), CompOSE Reference Manual, *Eur. Phys. J. A* **58**, 221 (2022).
 - [4] P. B. Demorest, T. Pennucci, S. M. Ransom, M. S. E. Roberts, and J. W. T. Hessels, A two-solar-mass neutron star measured using Shapiro delay, *Nature* **467**, 1081 (2010).
 - [5] J. Antoniadis *et al.*, A Massive Pulsar in a Compact Relativistic Binary, *Science* **340**, 448 (2013).
 - [6] Z. Arzoumanian *et al.* (NANOGrav), The NANOGrav 11-year Data Set: High-precision timing of 45 Millisecond Pulsars, *Astrophys. J., Suppl. Ser.* **235**, 37 (2018).
 - [7] H. T. Cromartie *et al.* (NANOGrav), Relativistic Shapiro delay measurements of an extremely massive millisecond pulsar, *Nat. Astron.* **4**, 72 (2020).
 - [8] E. Fonseca *et al.*, Refined Mass and Geometric Measurements of the High-mass PSR J0740+6620, *Astrophys. J. Lett.* **915**, L12 (2021).
 - [9] B. P. Abbott *et al.* (The LIGO Scientific Collaboration and the Virgo Collaboration), Gw170817: Measurements of neutron star radii and equation of state, *Phys. Rev. Lett.* **121**, 161101 (2018).
 - [10] B. P. Abbott *et al.* (LIGO Scientific Collaboration and Virgo Collaboration), Properties of the binary neutron star merger gw170817, *Phys. Rev. X* **9**, 011001 (2019).
 - [11] T. E. Riley *et al.*, A NICER View of PSR J0030+0451: Millisecond Pulsar Parameter Estimation, *Astrophys. J. Lett.* **887**, L21 (2019).
 - [12] M. C. Miller *et al.*, PSR J0030+0451 Mass and Radius from NICER Data and Implications for the Properties of Neutron Star Matter, *Astrophys. J. Lett.* **887**, L24 (2019).
 - [13] T. E. Riley *et al.*, A NICER View of the Massive Pulsar PSR J0740+6620 Informed by Radio Timing and XMM-Newton

¹ The documentation is available at <https://emcee.readthedocs.io> and the GitHub page is <https://github.com/dfm/emcee>.

² The documentation is available at <https://emcee.readthedocs.io/en/v2.2.1/user/pt/> and the GitHub page is <https://github.com/willvouden/ptmcee>. Note that `PTMCEE` is no longer maintained.

³ The documentation is available at <https://johannesbuchner.github.io/UltraNest/> and the GitHub page is <https://github.com/JohannesBuchner/UltraNest>.

- Spectroscopy, *Astrophys. J. Lett.* **918**, L27 (2021).
- [14] M. C. Miller *et al.*, The Radius of PSR J0740+6620 from NICER and XMM-Newton Data, *Astrophys. J. Lett.* **918**, L28 (2021).
 - [15] G. Raaijmakers, S. K. Greif, K. Hebeler, T. Hinderer, S. Nisanke, A. Schwenk, T. E. Riley, A. L. Watts, J. M. Lattimer, and W. C. G. Ho, Constraints on the Dense Matter Equation of State and Neutron Star Properties from NICER's Mass-Radius Estimate of PSR J0740+6620 and Multimessenger Observations, *Astrophys. J. Lett.* **918**, L29 (2021).
 - [16] S. Traversi, P. Char, and G. Pagliara, Bayesian inference of dense matter equation of state within relativistic mean field models using astrophysical measurements, *Astrophys. J.* **897**, 165 (2020).
 - [17] T. Malik, M. Ferreira, M. B. Albino, and C. Providência, Spanning the full range of neutron star properties within a microscopic description, *Phys. Rev. D* **107**, 103018 (2023).
 - [18] J. Zhou, J. Xu, and P. Papakonstantinou, Bayesian inference of neutron-star observables based on effective nuclear interactions, *Phys. Rev. C* **107**, 055803 (2023).
 - [19] S. M. A. Imam, T. Malik, C. Providência, and B. K. Agrawal, Implications of comprehensive nuclear and astrophysics data on the equations of state of neutron star matter, (2024).
 - [20] T. Malik, M. Ferreira, B. K. Agrawal, and C. Providência, Relativistic Description of Dense Matter Equation of State and Compatibility with Neutron Star Observables: A Bayesian Approach, *Astrophys. J.* **930**, 17 (2022).
 - [21] M. V. Beznogov and A. R. Raduta, Bayesian inference of the dense matter equation of state built upon covariant density functionals, *Phys. Rev. C* **107**, 045803 (2023).
 - [22] P. Char, C. Mondal, F. Gulminelli, and M. Oertel, Generalized description of neutron star matter with a nucleonic relativistic density functional, *Phys. Rev. D* **108**, 103045 (2023).
 - [23] M. V. Beznogov and A. R. Raduta, Bayesian Survey of the Dense Matter Equation of State built upon Skyrme effective interactions, arXiv e-prints, arXiv:2308.15351 (2023).
 - [24] X. L. Shang, A. Li, Z. Q. Miao, G. F. Burgio, and H.-J. Schulze, Nucleon effective mass in hot dense matter, *Phys. Rev. C* **101**, 065801 (2020).
 - [25] R. Somasundaram, C. Drischler, I. Tews, and J. Margueron, Constraints on the nuclear symmetry energy from asymmetric-matter calculations with chiral NN and $3N$ interactions, *Phys. Rev. C* **103**, 045803 (2021).
 - [26] M. Duan and M. Urban, Energy and angle dependence of neutrino scattering rates in proto-neutron star and supernova matter within Skyrme RPA, *Phys. Rev. C* **108**, 025813 (2023).
 - [27] S. Vinciguerra, T. Salmi, A. L. Watts, D. Choudhury, T. E. Riley, P. S. Ray, S. Bogdanov, Y. Kini, S. Guillot, D. Chakrabarty, W. C. G. Ho, D. Huppenkothen, S. M. Morsink, Z. Wadiasingh, and M. T. Wolff, An Updated Mass-Radius Analysis of the 2017–2018 NICER Data Set of PSR J0030+0451, *Astrophys. J.* **961**, 62 (2024).
 - [28] N. Chamel, S. Goriely, and J. M. Pearson, Further explorations of Skyrme-Hartree-Fock-Bogoliubov mass formulas. XI. Stabilizing neutron stars against a ferromagnetic collapse, *Phys. Rev. C* **80**, 065804 (2009).
 - [29] J. W. Negele and D. Vautherin, Density-matrix expansion for an effective nuclear hamiltonian, *Phys. Rev. C* **5**, 1472 (1972).
 - [30] C. Ducoin, P. Chomaz, and F. Gulminelli, Role of isospin in the nuclear liquid-gas phase transition, *Nucl. Phys. A* **771**, 68 (2006).
 - [31] S. Goriely, N. Chamel, and J. M. Pearson, Further explorations of Skyrme-Hartree-Fock-Bogoliubov mass formulas. XIII. The 2012 atomic mass evaluation and the symmetry coefficient, *Phys. Rev. C* **88**, 024308 (2013).
 - [32] S. Goriely, Further explorations of Skyrme-Hartree-Fock-Bogoliubov mass formulas. XV: The spin-orbit coupling, *Nucl. Phys. A* **933**, 68 (2015).
 - [33] M. Baldo, G. F. Burgio, H.-J. Schulze, and G. Taranto, Nucleon effective masses within the Brueckner-Hartree-Fock theory: Impact on stellar neutrino emission, *Phys. Rev. C* **89**, 048801 (2014).
 - [34] L.-W. Chen, B.-J. Cai, C. M. Ko, B.-A. Li, C. Shen, and J. Xu, Higher-order effects on the incompressibility of isospin asymmetric nuclear matter, *Phys. Rev. C* **80**, 014322 (2009).
 - [35] J. Margueron, R. Hoffmann Casali, and F. Gulminelli, Equation of state for dense nucleonic matter from metamodeling. I. Foundational aspects, *Phys. Rev. C* **97**, 025805 (2018).
 - [36] P. Haensel, J. L. Zdunik, and J. Dobaczewski, Composition and equation of state of cold catalyzed matter below neutron drip, *Astron. Astrophys.* **222**, 353 (1989).
 - [37] J. Negele and D. Vautherin, Neutron star matter at sub-nuclear densities, *Nucl. Phys. A* **207**, 298 (1973).
 - [38] M. C. Miller *et al.*, The Radius of PSR J0740+6620 from NICER and XMM-Newton Data, *Astrophys. J. Lett.* **918**, L28 (2021).
 - [39] T. Hinderer, Tidal love numbers of neutron stars, *Astrophys. J.* **677**, 1216 (2008).
 - [40] T. Hinderer, B. D. Lackey, R. N. Lang, and J. S. Read, Tidal deformability of neutron stars with realistic equations of state and their gravitational wave signatures in binary inspiral, *Phys. Rev. D* **81**, 123016 (2010).
 - [41] M. Dutra, O. Lourenço, J. S. Sá Martins, A. Delfino, J. R. Stone, and P. D. Stevenson, Skyrme interaction and nuclear matter constraints, *Phys. Rev. C* **85**, 035201 (2012).
 - [42] D. Foreman-Mackey, D. W. Hogg, D. Lang, and J. Goodman, emcee: The MCMC Hammer, *Publ. Astron. Soc. Pac.* **125**, 306 (2013).
 - [43] D. Foreman-Mackey, W. Farr, M. Sinha, A. Archibald, D. Hogg, J. Sanders, J. Zuntz, P. Williams, A. Nelson, M. de Val-Borro, T. Erhardt, I. Pashchenko, and O. Pla, emcee v3: A Python ensemble sampling toolkit for affine-invariant MCMC, *J. Open Source Software* **4**, 1864 (2019).
 - [44] J. Goodman and J. Weare, Ensemble samplers with affine invariance, *Comm. App. Math. and Comp. Sci.* **5**, 65 (2010).
 - [45] W. D. Voudsen, W. M. Farr, and I. Mandel, Dynamic temperature selection for parallel tempering in Markov chain Monte Carlo simulations, *Mon. Not. R. Astron. Soc.* **455**, 1919 (2016).
 - [46] J. Skilling, Nested Sampling, in *Bayesian Inference and Maximum Entropy Methods in Science and Engineering: 24th International Workshop on Bayesian Inference and Maximum Entropy Methods in Science and Engineering*, American Institute of Physics Conference Series, Vol. 735, edited by R. Fischer, R. Preuss, and U. V. Toussaint (2004) pp. 395–405.
 - [47] J. Skilling, Nested sampling for general Bayesian computation, *Bayesian Analysis* **1**, 833 (2006).
 - [48] J. Buchner, A statistical test for Nested Sampling algorithms, *Stat. Comput.* **26**, 383 (2016).
 - [49] J. Buchner, Collaborative Nested Sampling: Big Data versus Complex Physical Models, *Publ. Astron. Soc. Pac.* **131**, 108005 (2019).
 - [50] J. Buchner, UltraNest - a robust, general purpose Bayesian inference engine, *J. Open Source Software* **6**, 3001 (2021).